Original Article

DOI: 10.5582/bst.2025.01113

Advancing hepatobiliary diagnosis and treatment using shortwave-infrared fluorescence imaging with ICG-C9

Kosuke Hatta[1], Ryota Tanaka[1,*], Kenjiro Kimura[1], Naoki Yamashita[2], Jie Li[2], Terufusa Kunisada[2], Takeaki Ishizawa[1]

[1] Department of Hepato-Biliary-Pancreatic Surgery, Osaka Metropolitan University Graduate School of Medicine, Osaka, Japan;
[2] R&D Technology Center, Tamron Co., Ltd., Saitama, Japan.

SUMMARY: Indocyanine green (ICG)-C9, a novel cyanine dye developed by the Center for Biosystems Dynamics Research at RIKEN, provides significant advantages over conventional ICG due to its detectability *via* shortwave-infrared (SWIR) fluorescence imaging. Unlike standard ICG, ICG-C9 facilitates SWIR imaging and displays therapeutic potential when conjugated with antibodies *in vivo*, suggesting broader applicability across various cancer types. This study evaluated the efficacy of SWIR fluorescence imaging with ICG-C9 in comparison with existing near-infrared (NIR) imaging techniques. We assessed excretion kinetics and the relationship between excitation and fluorescence wavelengths for ICG-C9 and ICG following intravenous administration in BALB/c-nu mice. Tumor uptake was evaluated using a cell-line-derived subcutaneous tumor model from HuH-7 cells, representing hepatocellular carcinoma. Variables including dose, administration route, and exposure time were optimized for comparison. Maximum fluorescence intensity for ICG-C9 was observed with an excitation wavelength of 915 nm and fluorescence emission wavelengths >950 nm within the SWIR spectrum. Both ICG-C9 and ICG followed similar excretion pathways, involving hepatic uptake and biliary excretion. Tumor uptake of ICG-C9 was confirmed under similar conditions to ICG. ICG-C9 demonstrates promising potential as an alternative to NIR fluorescence imaging with ICG, offering unique properties that may enhance imaging capabilities. However, further research is required to establish its clinical applicability and broader therapeutic utility.

Keywords: shortwave-infrared, near-infrared, fluorescence imaging, indocyanine green, hepatocellular carcinoma

1. Introduction

The Center for Biosystems Dynamics Research at RIKEN has developed indocyanine green (ICG)-based π-conjugation-extended cyanine dyes, specifically ICG-C9 and ICG-C11. These dyes emit fluorescence in the shortwave-infrared (SWIR) spectrum at wavelengths of 922 nm and 1,010 nm, respectively, when dissolved in water. Using antibody conjugates with ICG-C9 and ICG-C11, researchers have demonstrated multiplexed SWIR fluorescence molecular imaging of breast tumors, visualizing both surface receptors and tumor vasculature in live mice (*1,2*).

Currently, near-infrared (NIR) fluorescence imaging with ICG is widely employed across various medical fields for diagnostic and therapeutic purposes (*3-7*). In hepatobiliary surgery, NIR fluorescence imaging has been utilized since its introduction (*8*), facilitating applications such as intraoperative fluorescence guidance and photodynamic therapy (*9-13*). Specifically, during laparoscopic cholecystectomy and hepatectomy for liver cancer, intraoperative NIR fluorescence imaging with ICG has been associated with a reduced risk of bile duct injuries (*14,15*) and improved patient prognosis (*16*). However, NIR imaging has limitations, including autofluorescence interference and inadequate visualization of deep tissues (*17,18*). In contrast, SWIR fluorescence imaging, operating within the 1,000 to 1,400 nm wavelength range, offers significant advantages, including reduced tissue absorption and light scattering. These properties allow for superior imaging of deeper tissues (*19,20*), enhancing its potential for diagnostic and therapeutic applications in oncology (*21-24*).

Despite growing interest in SWIR fluorescence imaging for hepatobiliary surgery, its clinical adoption remains limited, primarily due to the lack of suitable imaging devices and fluorescent probes (*25*). To address this gap, this study evaluates the potential of SWIR fluorescence imaging with ICG-C9 as an effective alternative to NIR imaging for hepatobiliary diseases.

We analyzed the fluorescence characteristics and pharmacokinetics of ICG-C9 and assessed its uptake in hepatocellular carcinoma models.

2. Materials and Methods

2.1. Equipment for fluorescence imaging system

The fluorescence imaging system used in this study comprised the following components: an industrial lens (SMA11F25, Tamron Co., Ltd., Saitama, Japan) capable of covering a broad spectral range from visible light to the SWIR band; three fluorescence filters supplied by Semrock Inc. (Rochester, NY, USA) — an 857 ± 15 nm band-pass filter (FF01-857), a 950 nm long-pass filter (FF01-937), and a 1000 nm long-pass filter (BLP01-980); a cooled monochrome SWIR camera (BH-71IGA, BITRAN Co., Ltd., Saitama, Japan) equipped with a SWIR image sensor (IMX990AABJ-C, Sony Semiconductor Solutions Co., Kanagawa, Japan); and two fiber-coupled lasers (HANGZHOU NAKU TECHNOLOGY Co., Ltd., Hangzhou, Zhejiang, China) with excitation wavelengths of 808 nm and 915 nm, along with beam expanders (ThorLabs Inc., Newton, NJ, USA). The fluorescence filters were used to detect emission wavelengths of 857 ± 15 nm, > 950 nm, and > 1,000 nm. The camera captured monochrome images corresponding to the red, green, and blue channels of the light emitted by the RGB light source (Leimac Co., Ltd, Tokyo, Japan), enabling the generation of RGB images. The lens was positioned 60 cm above the targets, and the light power density was maintained at 20 mW/cm² (Supplementary Figures S1 and S2, *https://www.biosciencetrends.com/action/getSupplementalData.php?ID=256*). Fluorescence intensity data were processed using ImageJ software (National Institutes of Health, NIH).

2.2. Fluorescence intensity of ICG and ICG-C9 *in vitro*

ICG and ICG-C9, kindly provided by Dr. Takashi Jin (Center for Biosystems Dynamics Research, RIKEN, Osaka, Japan), were dissolved in 1% bovine serum albumin (BSA) to a final concentration of 0.1 mg/mL. Fluorescence intensities of both dyes were measured for all combinations of excitation wavelengths (808 nm and 915 nm) and emission wavelengths (840–873 nm, > 950 nm, and >1,000 nm). The exposure time for all measurements was standardized at 30 ms.

2.3. Animals

BALB/c nude mice aged 5–6 weeks (n = 18) were procured from Oriental Yeast Co., Ltd. (Tokyo, Japan). The mice were housed under specific pathogen-free conditions, maintained at a 12-hour light/dark cycle, and provided with autoclaved food and tap water throughout the study. Anesthesia was induced with 3% isoflurane and maintained at 1–2% isoflurane during implantation procedures and intravenous injections. The animal experimental protocol was reviewed and approved by the Institutional Animal Care and Use Committee (Approval no. 23061), adhering to Japanese regulations and ethical guidelines for animal experimentation. Humane euthanasia was performed under isoflurane anesthesia prior to autopsy.

2.4. Pharmacokinetics of ICG and ICG-C9

ICG and ICG-C9 were prepared as solutions in 1% BSA in water and administered intravenously to 12 mice. Six mice received ICG and six received ICG-C9. A bolus injection of 0.5 mg/kg in 100 μL of water was delivered *via* the tail vein. Post-administration, mice were euthanized at predetermined intervals — 15 min, 30 min, 3 h, 6 h, and 24 h — to evaluate the distribution of the fluorescent dyes in excretory organs. Imaging was conducted as follows: Mice injected with ICG were imaged using an excitation wavelength of 808 nm and emission wavelengths ranging from 840 to 873 nm. Mice injected with ICG-C9 were imaged using an excitation wavelength of 915 nm and emission wavelengths > 950 nm. The exposure time for all imaging procedures was set to 30 ms.

2.5. Tumor cell line and xenograft model

HuH-7 cells, a well-differentiated human hepatoma cell line (*26*), were obtained from the Japanese Collection of Research Bioresources (JCRB) Cell Bank (Osaka, Japan). The cells were cultured in Dulbecco's Modified Eagle's Medium (DMEM, #044-29765, Fujifilm Wako, Tokyo, Japan) supplemented with 10% fetal bovine serum (FBS, #175012, Nichirei Bioscience, Tokyo, Japan) and 1% penicillin–streptomycin (P/S, #168-23191, Fujifilm Wako, Tokyo, Japan) and incubated at 37°C in a humidified atmosphere containing 5% CO_2 and 95% air. For harvesting, cells were briefly treated with 0.25% (w/v) trypsin–1 mmol/L EDTA solution (#209-16941, Fujifilm Wako, Tokyo, Japan).

After continuous culture, HuH-7 cells were collected into tubes, washed with phosphate-buffered saline (PBS, #045-29795, Fujifilm Wako, Tokyo, Japan), and resuspended in serum-free medium. Each mouse received a subcutaneous injection of 5×10^6 HuH-7 cells in 0.1 mL of serum-free medium containing 33% Matrigel (#356234, Corning, Tokyo, Japan) into the left flank.

2.6. Fluorescence imaging of subcutaneous xenograft models

ICG and ICG-C9 were administered intravenously *via* the tail vein to six mice (three mice per dye) once tumor sizes reached approximately 200 mm³, around three

weeks after HuH-7 cell transplantation. Fluorescence imaging was performed 24 h post-administration. The dyes were delivered as bolus injections at doses of 0.5, 2.5, or 7.5 mg/kg in volumes of 100, 100, and 300 µL of water, respectively. To avoid hemodynamic instability (*27*), the 7.5 mg/kg dose in a 300 µL volume was divided into three 100 µL aliquots and administered over a period of three days (100 µL/day). Tumors were excised from the mice after euthanasia and imaged using fluorescence techniques. Tumors from mice treated with ICG were imaged with an excitation wavelength of 808 nm and an emission range of 840–873 nm, whereas those from mice treated with ICG-C9 were imaged with an excitation wavelength of 915 nm and an emission range of > 950 nm. For each condition, images were acquired with exposure times of 30, 80, and 300 ms.

2.7. Fluorescence microscopy

The cellular uptake of ICG and ICG-C9 in tumors derived from the HuH-7 human hepatoma cell line was evaluated using fluorescence microscopy. Tumors were harvested from mice administered 7.5 mg/kg of either ICG or ICG-C9. Pathological specimens were fixed in formalin, sectioned into 7 µm slices, and stained with hematoxylin and eosin (H&E). Fluorescence microscopy images were acquired using a BZ-X810 microscope (Keyence, Osaka, Japan). The exposure time for image acquisition was set to 3 s. Composite images were generated by stitching multiple images captured with a 20× objective lens, utilizing the integrated imaging system of the microscope. To directly visualize fluorescence signals in the specimens without using fluorescent antibodies, an ICG filter (OP-87767; Keyence) was employed. This filter provided a 710–760 nm excitation window and an 810–875 nm emission window, enabling NIR imaging.

3. Results

3.1. Fluorescence intensity of ICG and ICG-C9 *in vitro*

For ICG, maximum fluorescence intensity was observed at an excitation wavelength of 808 nm, with emission wavelengths ranging from 840 to 873 nm. Fluorescence intensity was significantly reduced at an excitation wavelength of 915 nm. In contrast, ICG-C9 exhibited maximum fluorescence intensity at an excitation

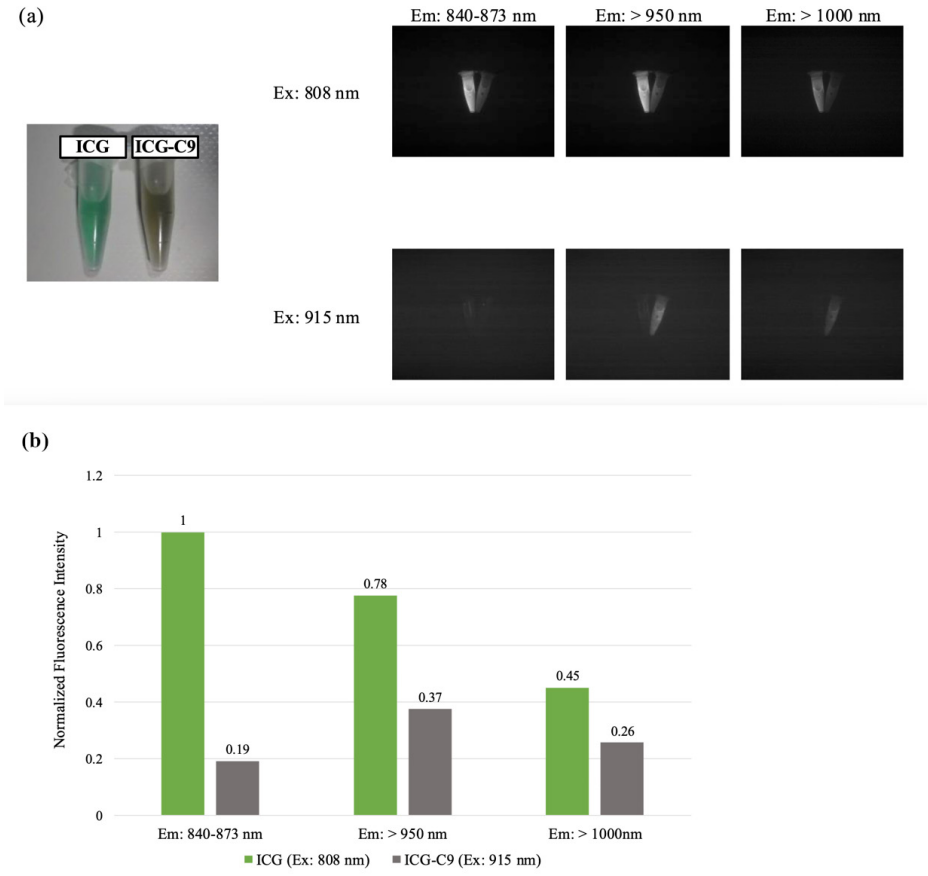

Figure 1. Fluorescence intensities of ICG and ICG-C9 (a) Fluorescence intensities were measured under various combinations of excitation wavelengths (808 nm and 915 nm) and emission wavelengths (840–873 nm, > 950 nm, and >1,000 nm), with an exposure time of 30 ms. **(b)** ICG showed maximum fluorescence intensity at an excitation wavelength of 808 nm and emission wavelengths of 840–873 nm. In contrast, ICG-C9 exhibited maximum fluorescence intensity at an excitation wavelength of 915 nm and emission wavelengths of > 950 nm. ICG-C9 exhibited weaker fluorescence intensity than ICG.

wavelength of 915 nm, with emission wavelengths exceeding 950 nm (Figure 1a). Despite maintaining consistent exposure times and light power intensities, ICG-C9 displayed weaker fluorescence intensity than ICG under these conditions (Figure 1b).

3.2. Pharmacokinetics of ICG and ICG-C9

Similar to ICG, ICG-C9 was selectively taken up from the bloodstream into the liver and rapidly excreted into the bile (Figure 2a). Fifteen min post-intravenous administration of ICG, hepatic fluorescence reached near-maximum levels, followed by excretion into the bile and distribution in the intestinal tract. After 3 h, intestinal fluorescence increased, while at 24 h, minimal fluorescence remained in the liver or intestinal tract. In contrast, 6 h post-administration of ICG-C9, fluorescence persisted in the liver, whereas ICG fluorescence was minimal (Figure 2b). These findings suggest that ICG-C9 displays a slower excretion rate than ICG.

3.3. Fluorescence imaging of subcutaneous xenograft models

Fluorescence from ICG or ICG-C9 was not detectable at low doses (0.5 mg/kg). ICG fluorescence was detectable at doses of 2.5 mg/kg or higher, while ICG-C9 required a dose of 7.5 mg/kg for detection (Figure 3a). The fluorescence intensity of ICG-C9 was lower than that of ICG; however, with an extended exposure time of 300 ms, ICG-C9 uptake became detectable. Both dyes were taken up into the HuH-7 human hepatoma cell line tumors, demonstrating similar tumor-targeting properties (Figure 3b).

3.4. Fluorescence microscopy

Fluorescence signals from both ICG and ICG-C9 were observed in HuH-7 tumors, confirming similar uptake characteristics at the microscopic level. Fluorescence localized to both tumor periphery and interior regions (Figure 4a). At the cellular level, fluorescence was

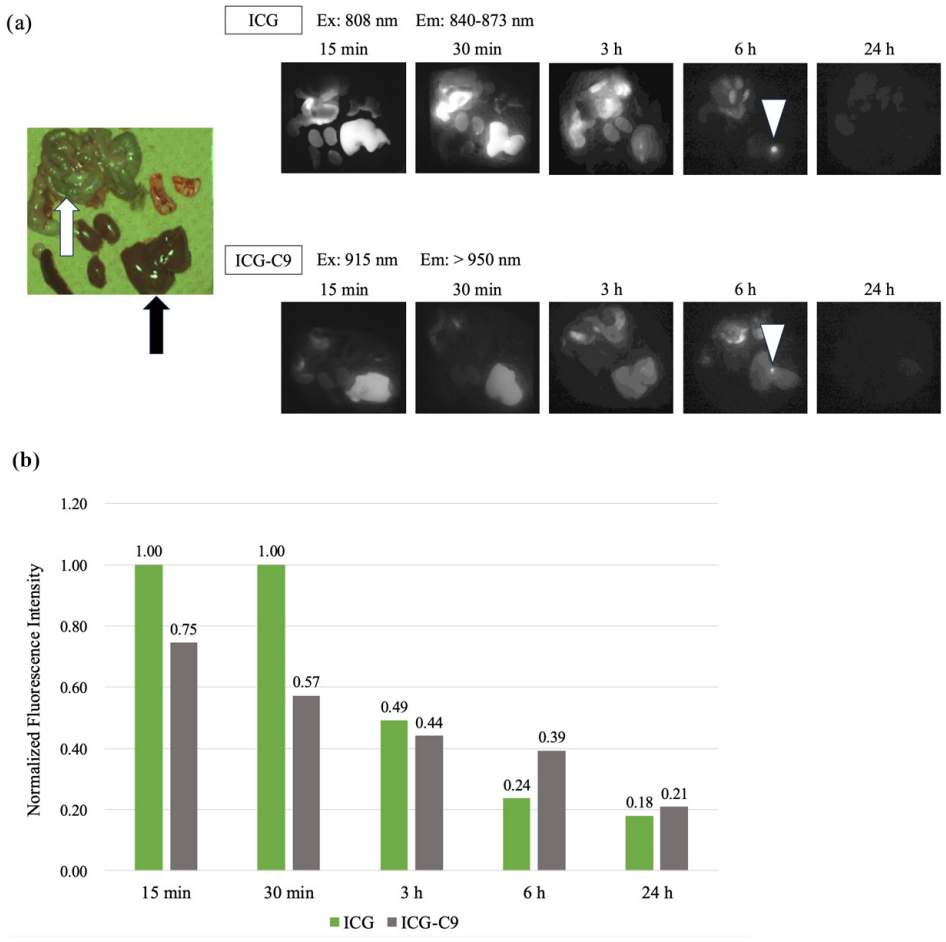

Figure 2. ICG and ICG-C9 distribution in excretory organs (a) Anatomical indicators: black arrow, liver; white arrow, intestine; white triangle, gallbladder. ICG and ICG-C9 were administered intravenously, and their distribution in excretory organs was analyzed at various time points post-administration. Both dyes were selectively taken up by the liver from the bloodstream and rapidly excreted into bile. No fluorescence signals were detectable in excretory organs 24 h after administration. **(b)** Fluorescence intensity in the liver following ICG and ICG-C9 administration. Six hours after ICG-C9 administration, detectable fluorescence persisted in the liver, whereas fluorescence from ICG was minimal. This suggests that ICG-C9 exhibits a slower excretion rate than ICG.

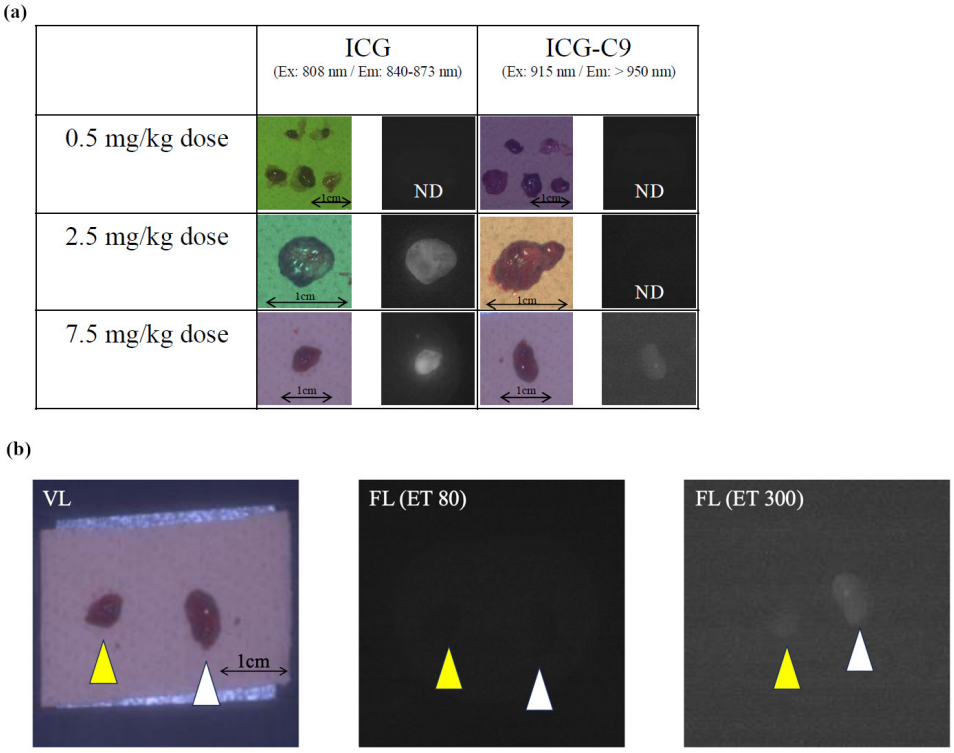

Figure 3. ICG and ICG-C9 uptake in tumors (a) Non-detectable (ND). A cell-line-derived subcutaneous tumor model from HuH-7 cells, representing hepatocellular carcinoma, was used to evaluate tumor uptake of ICG-C9 and compare it with ICG uptake. Fluorescence imaging was conducted 24 h post-administration. Tumors from mice treated with ICG were imaged using an excitation wavelength of 808 nm and emission wavelengths ranging from 840 to 873 nm, whereas tumors treated with ICG-C9 were imaged using an excitation wavelength of 915 nm and emission wavelengths of > 950 nm. ICG was detectable at a dose of 2.5 mg/kg with a 30 ms exposure time, whereas ICG-C9 required a dose of 7.5 mg/kg and a 300 ms exposure time for detection. **(b)** Panels: Left — tumors under visible light; center — fluorescence imaging with an 80 ms exposure time; right — fluorescence imaging with a 300 ms exposure time. A yellow triangle identifies a tumor from a mouse treated with ICG, while a white triangle marks a tumor from a mouse treated with ICG-C9. Fluorescence intensity for ICG-C9 was lower compared with ICG. Additionally, ICG-C9 was only detectable under the longer exposure time (300 ms), demonstrating that, like ICG, ICG-C9 is taken up by HuH-7-derived tumors.

predominantly found in the cytoplasm of HuH-7 cells, with no fluorescence observed in the nucleus (Figure 4b). The fluorescence intensity of ICG-C9 was lower than that of ICG, likely due to the shorter excitation and emission wavelength range of the filter used.

4. Discussion

This study highlights several advantages of ICG-C9, making it a promising alternative to conventional ICG for fluorescence imaging. One of the primary advantages of ICG-C9 is its fluorescence properties, with peak intensity achieved at an excitation wavelength of 915 nm and emission wavelengths > 950 nm in the SWIR spectrum. Moreover, ICG-C9 is one of the few biocompatible and water-soluble SWIR fluorescent probes, making it suitable for biomedical research and holding great potential to accelerate the clinical translation of SWIR fluorescence imaging. However, ICG-C9 exhibits lower fluorescence intensity than ICG under identical excitation density and exposure conditions due to its reduced quantum yield in aqueous solutions (*2*). Consequently, achieving optimal fluorescence with ICG-C9 may require higher doses, extended exposure times, or increased excitation light intensity. In this study, detectable fluorescence from the HuH-7 cell line tumor model was achieved with a dose of 7.5 mg/kg and an exposure time of 300 ms, while shorter exposure times (*e.g.*, 80 ms or less) resulted in insufficient fluorescence. While the required dose (7.5 mg/kg) and exposure time (300 ms) used in this study may not be directly applicable to real-time surgical imaging, our findings suggest potential for improving signal detection by adjusting excitation power and exposure conditions.

ICG-C9 shares similar excretion properties with ICG, with both being taken up by the liver from the bloodstream and excreted into bile. This characteristic enables intraoperative fluorescence cholangiography following intravenous administration of ICG-C9, as the excreted dye emits a fluorescence signal. Currently, intraoperative NIR fluorescence imaging using ICG during laparoscopic cholecystectomy is used to visualize biliary structures (*8,28*), reducing the risk of bile duct injuries (*14,15*). However, its effectiveness can be limited in patients with obesity or cholecystitis due to increased tissue thickness around the biliary structures (*29,30*). SWIR fluorescence, in contrast, displays reduced tissue absorption and scattering and

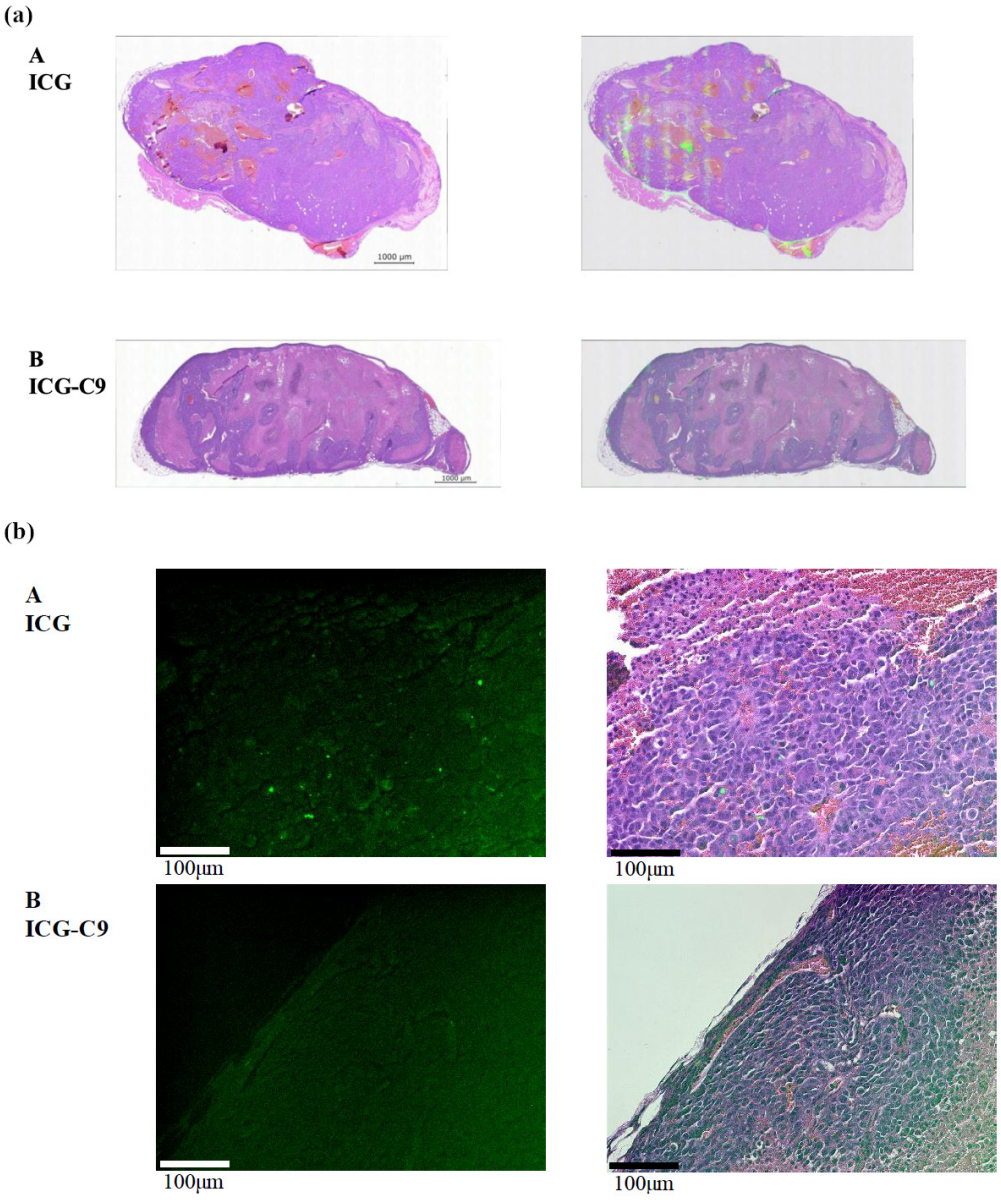

Figure 4. Microscopical analysis of tumors from mice administered 7.5 mg/kg doses of ICG or ICG-C9 (a) Left panel: cancer tissues stained with hematoxylin and eosin (H&E). Right panel: merged images showing fluorescence from ICG (A) or ICG-C9 (B) within cancer tissues. Both ICG and ICG-C9 demonstrated fluorescence within HuH-7 tumors, confirming similar uptake properties at the microscopic level. Fluorescence was localized to both the tumor periphery and interior regions. **(b)** Left panel: fluorescence images under a 20× objective lens. Right panel: merged images showing fluorescence. For both ICG and ICG-C9, fluorescence was confined to the cytoplasm of HuH-7 cells, with no signal detected in the nucleus.

is less affected by autofluorescence (*19,20*). This makes ICG-C9 particularly suited for deep tissue visualization. Nevertheless, the bile excretion properties of ICG-C9 may pose challenges, such as excessive liver background fluorescence, which could obscure bile duct visualization (*31,32*). The extended π-conjugated system of ICG-C9 increases its hydrophobicity, enhancing stronger protein and membrane binding (*2*). Although this leads to greater tissue accumulation, it also results in slower excretion, which may contribute to prolonged background fluorescence. Moreover, our findings suggest that ICG-C9 exhibits slower excretion compared to conventional ICG. However, like ICG, hepatic washout following administration was observed. This indicates that employing a delayed imaging protocol—allowing sufficient time after administration—may enhance tumor-to-background contrast and reduce interference with bile duct visualization. In clinical practice, ICG-C9 may need to be administered earlier than the typical timing used for ICG. Nevertheless, further investigation is required to determine the optimal timing of administration for effective imaging.

A significant advantage of ICG-C9 is its ability to accumulate in HuH-7 human hepatoma cell line tumors, similar to ICG. The mechanism by which ICG highlights hepatocellular carcinoma (HCC)

involves the retention of ICG within the tumor after it is washed out from the surrounding liver tissue. This occurs because well-differentiated HCC maintains the expression of ICG uptake transporters, such as Na^+/taurocholate cotransporting polypeptide and organic anion-transporting polypeptide 8, although at lower levels than normal liver tissue. However, morphological and functional impairments in the biliary excretion system within HCC prevent the efficient elimination of ICG, leading to its accumulation in the tumor (*33*). This mechanism has also been demonstrated in subcutaneous tumor mouse models using HuH-7 cells (*13*). The transporters involved in the uptake of ICG-C9 remain unknown; however, this study suggests that ICG-C9 shares bile excretory properties similar to those of ICG. Utilizing bile stasis around the tumor, ICG-C9 may enhance the sensitivity of intraoperative fluorescence imaging techniques for poorly differentiated HCC and liver metastases, allowing fluorescent visualization of tumor rims (*10,34*). SWIR imaging has been shown to provide higher sensitivity and improved target-to-background contrast when compared with NIR imaging, thereby making it a powerful tool for guiding liver cancer resections (*25*). Given that ICG-C9 exhibits its most intense fluorescence in the SWIR spectrum, it holds great potential for enhancing tumor imaging during surgery. Specifically, the combination of conventional NIR imaging using ICG and SWIR imaging using ICG-C9 may enable double-color imaging—such as distinguishing cancerous tissue from hepatic segments (*10,35*) and visualizing bile ducts and blood vessels (*8,28*). Similar to how ICG fluorescence imaging enables real-time, high-sensitivity detection of small, grossly unidentifiable liver tumors (*10*), it may facilitate the identification of deeper or previously undetectable lesions. Additionally, studies have demonstrated the utility of ICG-labeled antibodies for target cell imaging with NIR fluorescence and for ICG-based phototherapy in hepatocellular carcinoma (*13,36*). These approaches could also be adapted to SWIR imaging with ICG-C9, enabling multi-color imaging by labeling different antibodies with ICG and ICG-C9 and switching excitation wavelengths (*2*). This capability could broaden therapeutic applications, including more precise and targeted cancer treatments.

Despite its potential, this study has several limitations. Although ICG-C9 is bile-excreted, its fluorescence intensity in macroscopic observations was weaker than expected, likely due to its inherently lower fluorescence intensity compared with ICG. Another potential factor could be the camera-to-object distance used in this experiment, which was substantially greater than the typical distance in conventional endoscopic or handheld fluorescence observation devices. In clinical practice, shorter distances between the imaging device and the target tissue are expected to enhance excitation light delivery and fluorescence signal capture, potentially improving the visibility of ICG-C9-labeled tumors. Therefore, the performance of ICG-C9 observed in our experimental setup may underestimate its true potential under surgical conditions. The large camera-to-object distance, relative to the size of the object, may have resulted in insufficient excitation or signal detection. Furthermore, the excitation light intensity used in this study (20 mW/cm^2) may have been relatively low, which could have further limited the efficiency of fluorescence excitation and detection. In this study, a cell line-derived subcutaneous xenograft model was used to evaluate the *in vivo* performance of ICG-C9. However, this model lacks the heterogeneity and biological complexity of actual patient tumor. Moreover, because the tumors were implanted subcutaneously, we were unable to assess fluorescence differences between tumor and paraneoplastic tissues. As a result, it remains unclear whether ICG-C9 was specifically taken up by tumor cells in this model. Additionally, the small sample size, and limited range of cell lines tested constrain the generalizability of the findings. Further research is warranted to investigate whether other human hepatoma cell lines exhibit similar preferential uptake of ICG-C9 and to confirm its utility in SWIR fluorescence imaging. To better replicate clinical conditions and evaluate tumor-specific uptake, future studies should incorporate patient-derived xenograft models that more accurately reflect the biological diversity of human tumors. Furthermore, liver transplant xenograft models would enable direct comparison between tumor and normal hepatocytes, providing more precise insights into the specificity of ICG-C9 accumulation. While ICG is considered a safe fluorescence dye (*37*), the cytotoxicity profile of ICG-C9 — though ICG-C9 exhibits a concentration-dependent cytotoxicity profile similar to conventional ICG based on the 3-(4,5-dimethylthiazol-2-yl)-2,5-diphenyltetrazolium bromide assays in HeLa cells (*2*) — requires further validation. Future studies should focus on characterizing the pharmacokinetics, tumor accumulation, and tissue penetration capabilities of SWIR light when using ICG-C9. Moreover, optimizing imaging parameters such as dose, exposure time, and excitation light intensity will be crucial for maximizing the clinical utility of SWIR imaging with ICG-C9.

In conclusion, our study demonstrated that ICG-C9, like ICG, is excreted *via* bile and exhibits fluorescence in the SWIR range. Additionally, ICG-C9 was effectively taken up by tumors derived from a human hepatoma cell line. These findings suggest that ICG-C9 holds potential for applications in hepatobiliary surgery and as a therapeutic agent when conjugated with antibodies. However, further studies are necessary to evaluate its safety, efficacy, and clinical utility. Addressing key issues such as fluorescence intensity, pharmacokinetics, and generalizability is essential to enhance the translational relevance of our study.

Acknowledgements

Authors acknowledge Dr. Takashi Jin (Center for Biosystems Dynamics Research, RIKEN, Osaka, Japan) for donating ICG and ICG-C9, and Keyence (Osaka, Japan) for microscopic imaging.

Funding: This study was supported by R&D Technology Center, Tamron Co. The study sponsor had no role in study design; in the collection, analysis, and interpretation of data; in the writing of the report; or in the decision to submit the paper for publication.

Conflict of Interest: R&D Technology Center, Tamron Co. provided the fluorescence imaging system for this study.

Data Availability Statement: The datasets generated and analyzed during the current study are available from the corresponding author upon reasonable request.

References

1. Swamy MMM, Murai Y, Monde K, Tsuboi S, Jin T. Shortwave-infrared fluorescent molecular imaging probes based on π-conjugation extended indocyanine green. Bioconjug Chem. 2021; 32:1541-1547.
2. Swamy MMM, Murai Y, Monde K, Tsuboi S, Swamy AK, Jin T. Biocompatible and water-soluble shortwave-infrared (SWIR)-emitting cyanine-based fluorescent probes for *in vivo* multiplexed molecular imaging. ACS Appl Mater Interfaces. 2024; 16:17253-17266.
3. Kitai T, Inomoto T, Miwa M, Shikayama T. Fluorescence navigation with indocyanine green for detecting sentinel lymph nodes in breast cancer. Breast Cancer. 2005; 12:211-215.
4. Kusano M, Tajima Y, Yamazaki K, Kato M, Watanabe M, Miwa M. Sentinel node mapping guided by indocyanine green fluorescence imaging: A new method for sentinel node navigation surgery in gastrointestinal cancer. Dig Surg. 2008; 25:103-108.
5. Ogata F, Azuma R, Kikuchi M, Koshima I, Morimoto Y. Novel lymphography using indocyanine green dye for near-infrared fluorescence labeling. Ann Plast Surg. 2007; 58:652-655.
6. Raabe A, Nakaji P, Beck J, Kim LJ, Hsu FP, Kamerman JD, Seifert V, Spetzler RF. Prospective evaluation of surgical microscope-integrated intraoperative near-infrared indocyanine green videoangiography during aneurysm surgery. J Neurosurg. 2005; 103:982-989.
7. Rubens FD, Ruel M, Fremes SE. A new and simplified method for coronary and graft imaging during CABG. Heart Surg Forum. 2002; 5:141-144.
8. Ishizawa T, Bandai Y, Kokudo N. Fluorescent cholangiography using indocyanine green for laparoscopic cholecystectomy: an initial experience. Arch Surg. 2009; 144:381-382.
9. Inoue Y, Arita J, Sakamoto T, Ono Y, Takahashi M, Takahashi Y, Kokudo N, Saiura A. Anatomical liver resections guided by 3-dimensional parenchymal staining using fusion indocyanine green fluorescence imaging. Ann Surg. 2015; 262:105-111.
10. Ishizawa T, Fukushima N, Shibahara J, Masuda K, Tamura S, Aoki T, Hasegawa K, Beck Y, Fukayama M, Kokudo N. Real-time identification of liver cancers by using indocyanine green fluorescent imaging. Cancer. 2009; 115:2491-2504.
11. Ishizawa T, Saiura A, Kokudo N. Clinical application of indocyanine green-fluorescence imaging during hepatectomy. Hepatobiliary Surg Nutr. 2016; 5:322-328.
12. Ishizawa T, Tamura S, Masuda K, Aoki T, Hasegawa K, Imamura H, Beck Y, Kokudo N. Intraoperative fluorescent cholangiography using indocyanine green: A biliary road map for safe surgery. J Am Coll Surg. 2009; 208:e1-e4.
13. Kaneko J, Inagaki Y, Ishizawa T, Gao J, Tang W, Aoki T, Sakamoto Y, Hasegawa K, Sugawara Y, Kokudo N. Photodynamic therapy for human hepatoma-cell-line tumors utilizing biliary excretion properties of indocyanine green. J Gastroenterol. 2014; 49:110-116.
14. Dip F, LoMenzo E, Sarotto L, *et al*. Randomized trial of near-infrared incisionless fluorescent cholangiography. Ann Surg. 2019; 270:992-999.
15. Pesce A, Piccolo G, La Greca G, Puleo S. Utility of fluorescent cholangiography during laparoscopic cholecystectomy: a systematic review. World J Gastroenterol. 2015; 21:7877-7883.
16. He K, Hong X, Chi C, Cai C, An Y, Li P, Liu X, Shan H, Tian J, Li J. Efficacy of near-infrared fluorescence-guided hepatectomy for the detection of colorectal liver metastases: a randomized controlled trial. J Am Coll Surg. 2022; 234:130-137.
17. Sordillo LA, Pu Y, Pratavieira S, Budansky Y, Alfano RR. Deep optical imaging of tissue using the second and third near-infrared spectral windows. J Biomed Opt. 2014; 19:056004.
18. Carr JA, Franke D, Caram JR, Perkinson CF, Saif M, Askoxylakis V, Datta M, Fukumura D, Jain RK, Bawendi MG, Bruns OT. Shortwave infrared fluorescence imaging with the clinically approved near-infrared dye indocyanine green. Proc Natl Acad Sci U S A. 2018; 115:4465-4470.
19. Ding F, Zhan Y, Lu X, Sun Y. Recent advances in near-infrared II fluorophores for multifunctional biomedical imaging. Chem Sci. 2018; 9:4370-4380.
20. Smith AM, Mancini MC, Nie S. Bioimaging: second window for *in vivo* imaging. Nat Nanotechnol. 2009; 4:710-711.
21. Suo Y, Wu F, Xu P, Shi H, Wang T, Liu H, Cheng Z. NIR-II fluorescence endoscopy for targeted imaging of colorectal cancer. Adv Healthc Mater. 2019; 8:e1900974.
22. Dai H, Shen Q, Shao J, Wang W, Gao F, Dong X. Small molecular NIR-II fluorophores for cancer phototheranostics. Innovation (Camb). 2021; 2:100082.
23. Iida T, Kiya S, Kubota K, Jin T, Seiyama A, Nomura Y. Monte Carlo modeling of shortwave-infrared fluorescence photon migration in voxelized media for the detection of breast cancer. Diagnostics (Basel). 2020; 10:961.
24. Fan X, Yang J, Ni H, Xia Q, Liu X, Wu T, Li L, Prasad PN, Liu C, Lin H, Qian J. Initial experience of NIR-II fluorescence imaging-guided surgery in foot and ankle surgery. Engineering. 2024; 40:19-27.
25. Hu Z, Fang C, Li B, *et al*. First-in-human liver-tumour surgery guided by multispectral fluorescence imaging in the visible and near-infrared-I/II windows. Nat Biomed Eng. 2020; 4:259-271.
26. Nakabayashi H, Taketa K, Miyano K, Yamane T, Sato J. Growth of human hepatoma cells lines with differentiated functions in chemically defined medium. Cancer Res.

1982; 42:3858-3863.
27. Diehl KH, Hull R, Morton D, Pfister R, Rabemampianina Y, Smith D, Vidal JM, van de Vorstenbosch C, European Federation of Pharmaceutical Industries Association and European Centre for the Validation of Alternative Methods. A good practice guide to the administration of substances and removal of blood, including routes and volumes. J Appl Toxicol. 2001; 21:15-23.
28. Dip F, Roy M, Menzo EL, Simpfendorfer C, Szomstein S, Rosenthal RJ. Routine use of fluorescent incisionless cholangiography as a new imaging modality during laparoscopic cholecystectomy. Surg Endosc. 2015; 29:1621-1626.
29. Daskalaki D, Fernandes E, Wang X, Bianco FM, Elli EF, Ayloo S, Masrur M, Milone L, Giulianotti PC. Indocyanine green (ICG) fluorescent cholangiography during robotic cholecystectomy: results of 184 consecutive cases in a single institution. Surg Innov. 2014; 21:615-621.
30. Igami T, Nojiri M, Shinohara K, Ebata T, Yokoyama Y, Sugawara G, Mizuno T, Yamaguchi J, Nagino M. Clinical value and pitfalls of fluorescent cholangiography during single-incision laparoscopic cholecystectomy. Surg Today. 2016; 46:1443-1450.
31. Esposito C, Alberti D, Settimi A, Pecorelli S, Boroni G, Montanaro B, Escolino M. Indocyanine green (ICG) fluorescent cholangiography during laparoscopic cholecystectomy using RUBINA™ technology: preliminary experience in two pediatric surgery centers. Surg Endosc. 2021; 35:6366-6373.
32. Kono Y, Ishizawa T, Tani K, Harada N, Kaneko J, Saiura A, Bandai Y, Kokudo N. Techniques of fluorescence cholangiography during laparoscopic cholecystectomy for better delineation of the bile duct anatomy. Medicine (Baltimore). 2015; 94:e1005.
33. Ishizawa T, Masuda K, Urano Y, Kawaguchi Y, Satou S, Kaneko J, Hasegawa K, Shibahara J, Fukayama M, Tsuji S, Midorikawa Y, Aburatani H, Kokudo N. Mechanistic background and clinical applications of indocyanine green fluorescence imaging of hepatocellular carcinoma. Ann Surg Oncol. 2014; 21:440-448.
34. van der Vorst JR, Hutteman M, Mieog JS, de Rooij KE, Kaijzel EL, Löwik CW, Putter H, Kuppen PJ, Frangioni JV, van de Velde CJ, Vahrmeijer AL. Near-infrared fluorescence imaging of liver metastases in rats using indocyanine green. J Surg Res. 2012; 174:266-271.
35. Ishizawa T, Zuker NB, Kokudo N, Gayet B. Positive and negative staining of hepatic segments by use of fluorescent imaging techniques during laparoscopic hepatectomy. Arch Surg. 2012; 147:393-394.
36. Jin T, Tsuboi S, Komatsuzaki A, Imamura Y, Muranaka Y, Sakata T, Yasuda H. Enhancement of aqueous stability and fluorescence brightness of indocyanine green using small calix[4]arene micelles for near-infrared fluorescence imaging. MedChemComm. 2016; 7:623-631.
37. Obana A, Miki T, Hayashi K, *et al*. Survey of complications of indocyanine green angiography in Japan. Am J Ophthalmol. 1994; 118:749-753.

Received April 14, 2025; Revised June 4, 2025; Accepted June 9, 2025.

**Address correspondence to:*
Ryota Tanaka, Department of Hepato-Biliary-Pancreatic Surgery, Osaka Metropolitan University Graduate School of Medicine, Osaka 545-8585, Japan.
E-mail: taanaakaa3364@gmail.com

Released online in J-STAGE as advance publication June 14, 2025.